ISSN 1063-7737, Astronomy Letters, 2022, Vol. 48, No. 8, pp. 447–454. © Pleiades Publishing, Inc., 2022.
Russian Text © The Author(s), 2022, published in Pis'ma v Astronomicheskii Zhurnal, 2022, Vol. 48, No. 8, pp. 568–576.

Simulations of Burning and Nucleosynthesis in a Thermonuclear Supernova

S. I. Glazyrin[1,2,3*] and I. V. Panov[1,4]**

[1]*"Kurchatov Institute" National Research Center, Moscow, 123182 Russia*
[2]*Dukhov All-Russian Research Institute of Automatics, Moscow, 127055 Russia*
[3]*Lebedev Physical Institute, Russian Academy of Sciences, Moscow, 119991 Russia*
[4]*Moscow Institute of Physics and Technology (National Research University), Dolgoprudnyi, 141701 Russia*

Received May 23, 2022; revised June 14, 2022; accepted June 20, 2022

Abstract—Nucleosynthesis at the deflagration stage of a white dwarf is considered. Burning calculations have been made with the previously developed hydrodynamic model implemented in the FRONT3D code including turbulence. The trajectories of passive particles used thereafter for nucleosynthesis simulations have been created through the hydrodynamic calculations. The abundances of elements from oxygen to iron and nickel calculated in the developed nucleosynthesis model are shown to be in agreement with both observations and calculations based on other models.

DOI: 10.1134/S1063773722080035

Keywords: *supernovae and supernova remnants, nuclear reactions, beta decay.*

1. INTRODUCTION

Supernovae (SNe) are significant events in the life of any galaxy. First, a large fraction of the energy of these objects being released goes away in the form of kinetic energy, maintaining the activity in galaxies and carrying away the remnant material into the surrounding medium. Second, explosive nucleosynthesis is responsible for the production of elements up to the iron peak. Given the high SN remnant expansion velocity, such events are important sources of new elements and affect the chemical evolution in the Universe.

The most realistic scenario for the explosion of type Ia supernovae (SNe Ia) is the thermonuclear burning of white dwarfs. In this case, the small variety of observed SN Ia explosion parameters (compared to other types of SNe) and the peculiarities of the observed spectrum can be explained. In particular, SNe Ia are distinguished by a strong Si II line in the spectrum in the absence of hydrogen and by a set of lines of other metals (Filippenko 1997). White dwarfs are degenerate stars and are composed predominantly of carbon and oxygen whose burning gives rise to silicon.

There are no active nuclear reactions at the center of isolated white dwarfs. Therefore, the burning that leads to an SN explosion must be initiated by some external action. Two initiation scenarios are usually distinguished, each of which is associated with binary systems (Whelan and Iben 1973; Webbink 1979, 1984; Iben and Tutukov 1984). The first is the collision of white dwarfs as a result of their gradual approach. This scenario is of great interest from the standpoint of nucleosynthesis, but is not considered in this paper. The second scenario is the instability of a white dwarf that arises as its mass approaches the limiting (Chandrasekhar) one. This occurs in a binary system with a nondegenerate component as a result of mass transfer onto a degenerate star. Because of the instability, the center of the white dwarf can heat up to an extent that a propagating burning front (flame) will arise. This burning even in a slow (subsonic) regime propagates with a high speed (a few percent of the speed of sound), causing the bulk of the star to burn out in a time of the order of a few seconds. The thermonuclear reactions proper begin at the burning front and the burnout continues behind the front (due to the high temperature). The structure of the burning front was investigated in a number of papers (see, e.g., Khokhlov 1995; Timmes and Woosley 1992; Hillebrandt and Niemeyer 2000), with the reaction network being limited by the α, x reactions. These reactions make a major contribution to the energy release whose proper calculation is important for reproducing the burning front structure. Most often these include the following main 16 in-

*E-mail: glazyrin@itep.ru
**E-mail: igor.panov@itep.ru

gredients: n, p, ^{4}He, ^{12}C, ^{16}O, ^{20}Ne, ^{24}Mg, ^{28}Si, ^{32}S, ^{36}Ar, ^{40}Ca, ^{44}Ti, ^{48}Cr, ^{52}Fe, ^{56}Ni, and ^{60}Zn. In some papers the number of ingredients increases to 383, as, for example, in the postprocessing calculations of Travaglio et al. (2004). We considered the same number of chemical elements, while the number of isotopes differed insignificantly. The model used in this paper considers all of the significant pair reactions from the database of Rauscher and Thielemann (2000).

The approach to the nucleosynthesis calculations presented in this paper consists of two parts. The first part is the stellar burning hydrodynamics. At this stage, the flame propagation through the star is calculated by taking into account its nonuniform density distribution. The hydrodynamic model of the first stage takes into account the influence of medium parameters and the development of flame instabilities on the burning speed. In addition, the dynamical expansion of the star due to the heating of its interior is taken into account in a consistent way. At the second stage the model of a detailed nuclear reaction network is added, which is used to calculate the synthesis of new isotopes during the evolution of certain medium particles that are transferred together with the flow. As a result, both the spatial distribution of the produced elements and their isotopic composition are determined. In this paper we restrict ourselves to the deflagration (subsonic) regime of stellar burning and nucleosynthesis at this stage. Such burning does not lead to a full-scale SN Ia explosion, but can explain some weak SN 2008ha-type explosions. In addition, in normal SNe Ia the deflagration stage precedes detonation and occurs mainly at the stellar center. Therefore, the presented results are valid for the central regions of the remnant.

The paper consists of several sections: the hydrodynamic stellar burning model is considered in Section 2, the results of applying this model to the burning of a Chandrasekhar-mass white dwarf are presented in Section 3, and the nucleosynthesis results are considered in Section 4.

2. THE HYDRODYNAMIC MODEL

In the developed hydrodynamic model (Glazyrin 2013) turbulence plays a significant role in the flame propagation. We investigate the star since the flame initiation, when weak turbulence is already present (the typical turbulence velocities are much lower than the flame propagation velocity). This turbulence arises at the stage of slow distributed burning that lasts hundreds of years and precedes the further explosive process leading to an SN explosion. Such weak turbulence is enhanced by the Rayleigh–Taylor–Landau instability (Rayleigh 1883; Taylor 1950; Landau 1944) that the flame front is subjected to (the density jump at the burning front is oppositely directed to the pressure jump that arises due to the gravitational forces in the star). The instability rapidly passes to the nonlinear stage and the mixing stage, which, as a result, accelerates the flame through enhanced heat transfer. In addition, turbulent diffusion causes the density jump to be smeared.

Direct numerical simulations of the burning front in which all of the necessary scales of the problem are resolved are inaccessible for the present-day numerical capabilities, since all of the effects of interest to us manifest themselves on the scales of the star that are larger than the flame thickness by many orders of magnitude. For this reason, the flame is treated as a thin surface on which the reactions and energy release occur. The burning speed on this surface (i.e., the flame speed in the reference frame of the reactants ahead of the front) is specified as an explicit function of the state of the medium. This function can be derived only from calculations in which the structure of the flame front obtained previously is resolved (Timmes and Woosley 1992).

To describe the influence of turbulence and its interaction with the flow and the flame, we used the so-called k–ϵ model that takes into account the energy of turbulent pulsations and its decay (see Glazyrin (2013) and references therein). For the current calculations it is important that this turbulence model reproduces well the mixing processes due to the Rayleigh–Taylor (RL) and Kelvin–Helmholtz (KH) instabilities. A big advantage of this model is that it reproduces well the average three-dimensional properties of turbulence in calculations with a lower spatial dimension. Note that a similar model (Simonenko et al. 2007) was used to describe the burning on the surface of neutron stars.

Let us briefly outline the equations of the burning model (the system of hydrodynamic equations with burning and the method of their solution were described in detail previously; see Glazyrin 2014):

$$\partial_t \rho + \partial_i(\rho v_i) = 0, \quad (1)$$

$$\partial_t(\rho v_i) + \partial_j\left(\rho v_i v_j + p\delta_{ij}\right) = -\partial_j R_{ij} + \rho g_i, \quad (2)$$

$$\partial_t E + \partial_i(v_i(E+p)) = -G_2 + \rho\epsilon + \partial_i(p a_i - Q_i^T). \quad (3)$$

The terms that describe the turbulent contribution to the dynamics are shown on the right-hand side of the equations: R_{ij} is the Reynolds tensor, G_2 is the turbulence generation term, a_i is the turbulent quantity proportional to the density gradient, ϵ is the turbulent energy dissipation rate, Q_i^T is the energy flux due to the thermal conductivity including the contribution of

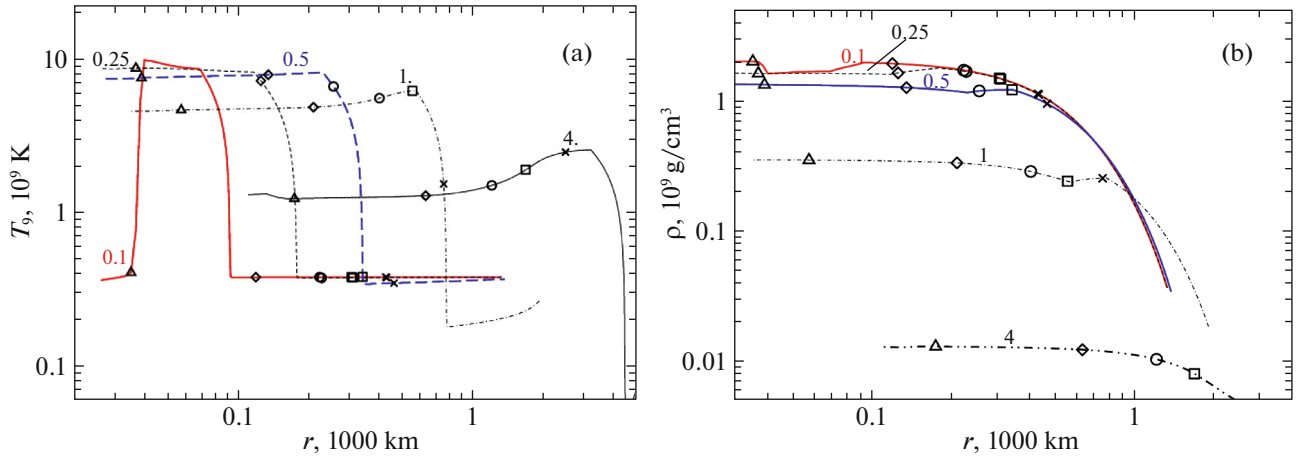

Fig. 1. White dwarf characteristics at different times after the onset of burning for the temperature profile (a) and the density profile (b). The code of the curves is the time in seconds. The signs denote the numbers of the passive particle trajectories along which detailed nucleosynthesis calculations are performed (triangle—5; diamond—100; circle—200; square—250; cross—300).

turbulent pulsations, and g_i is the gravitational acceleration. The emerging turbulence affects significantly the flame dynamics and the burning speed, increasing it by several orders of magnitude.

During stellar burning the characteristic burning time scale at the flame front is much shorter than the hydrodynamic time. This means that the flame may be treated as a thin surface separating the burnt material from the unburnt one. In this case, the front is described by a surface that moves with a normal velocity u_n relative to the material at rest. In the one-dimensional case, the radius of the burning front is described by the dynamical equation

$$\frac{dR_b}{dt} = v(R_b) + u_n(\rho(R_b), T(R_b), k_{\rm turb}(R_b)). \quad (4)$$

Since the flame front is not resolved in details (with the burning structure), the burning speed is specified as a function of medium parameters. This function itself was derived from microscopic simulations of the burning front and takes into account the turbulent corrections (via the energy of turbulent pulsations $k_{\rm turb}$). In the general 3D case, the equations defining the burning dynamics are described, for example, in Reinecke et al. (1999). This approach does not require a high spatial resolution and the results of the burning calculations at the hydrodynamic stage depend weakly on this resolution.

3. WHITE DWARF BURNING

According to the scenario for the explosion of SNe Ia with one degenerate component, the explosion occurs in the star that becomes unstable when the Chandrasekhar mass limit $M \approx 1.4\ M_\odot$ is reached. The central density of such stars is a few 10^9 g cm^{-3}.

The flame initiation mechanism is fairly complex and is related to the long prehistory of slow burning in the central part of the star. This stage cannot be described by the model that is used to describe the SN explosion and, therefore, the characteristic parameters of the flow in the star were taken from the calculations of Nonaka et al. (2012). According to these calculations, slow burning occurs in a turbulent medium with a turbulent intensity $v' = 16$ km s^{-1} and an integral length scale of turbulent eddies $L = 200$ km, while the initial flame position is offset from the center by $r = 50$ km.

In our calculations we considered a star with a central density $\rho_c = 2 \times 10^9$ g cm^{-3}, which is a fairly typical value. Since at such a density and a temperature of several thousand kelvins the material is in a strongly degenerate state, knowing ρ_c for the initial chemical composition (we assume that 0.5^{12}C + 0.5^{16}O by mass) allows the stellar structure to be obtained by integrating the steady-state hydrodynamic equations.

Figure 1 shows the computed spatial density and temperature profiles at different times. In the model used the position of the flame front is known explicitly. On the plots of the temperature and density profiles the advance of the burning front is noticeable by the growth of $T_9(t)$ and $\rho(t)$ (this is particularly clearly seen on the temperature profiles for $t = 1$ and 4 s and for the density at $t = 0.1$, 0.5, and 1 s). The turbulence that emerges near the flame due to the Rayleigh–Taylor–Landau instability development causes the temperature profiles to be smeared. At the initial time the flame propagates in both directions (inward and outward of the star). For $t = 0.1$ s there are two jumps in temperature (there are similar jumps in density, but they are less distinct). The

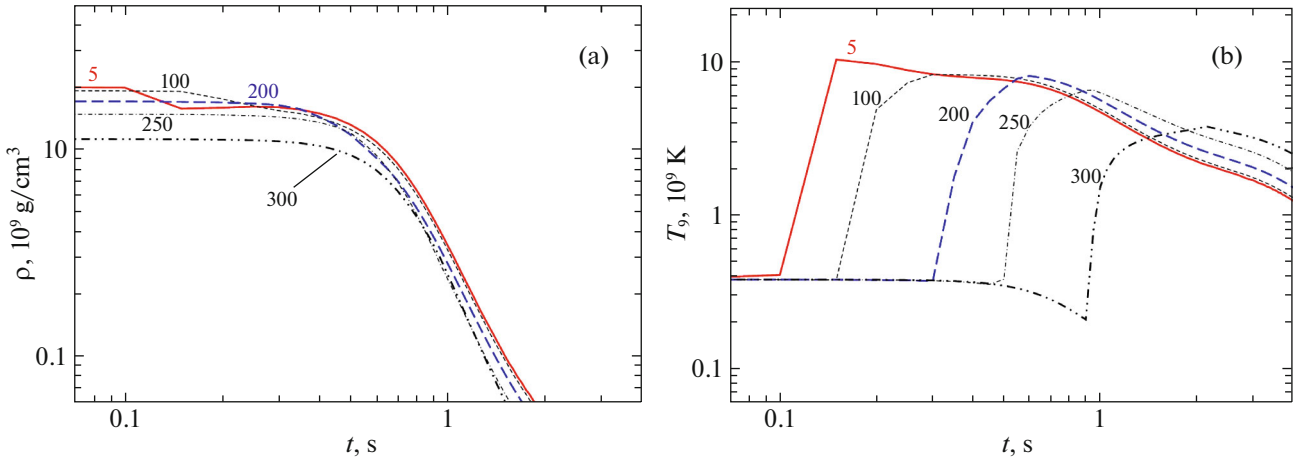

Fig. 2. Temporal changes in density (a) and temperature (b) for five typical trajectories of passive particles. The code of the curves is the passive particle trajectory number. The numbering begins from the stellar center.

inner flame front rapidly reaches the center because of its high velocity at a high density of the material. The outer burning front exerts a major effect on the stellar dynamics. Since the burning speed is low with respect to the speed of sound, the star expands and its mean density drops. At each time the star manages to adjust to quasi-static equilibrium.

The burning speed depends, on the one hand, on the density of the medium and, on the other hand, on the intensity of turbulence, which is enhanced with time, maintaining a high burning rate.

Since we consider only the deflagration stage of burning, the speeds of the material remain subsonic and the kinetic energy of the remnant is low: in the presented calculations it is $E_{\rm kin} \approx 1.6 \times 10^{49}$ erg at $t = 4$ s. A transition to detonation would lead to a significant acceleration of the material (by an order of magnitude).

The nucleosynthesis calculations were performed at the postprocessing stage at several Lagrangian points. For their implementation we used the algorithm of passive particles in the white dwarf explosion calculations, which allowed us to obtain the parameter evolution trajectories comoving with the medium of passive particles along which the nucleosynthesis was calculated.

From the hydrodynamic white dwarf burning calculations we chose the most typical trajectories whose Lagrangian points at the initial time had different distances from the stellar center (from 37 km for trajectory no. 5 to 430 km from trajectory no. 300). These trajectories were used for the nucleosynthesis simulations. The positions of the Lagrangian points at different times in the course of stellar evolution are presented in Fig. 1.

In Fig. 1 the signs indicate the set of passive particles that represent a typical sample of trajectories. The arrangement of the signs covers a great variety of conditions through the star and allows the difference in burning wave arrival time to be taken into account. These particles at the ignition time are at different distances from the stellar center and, therefore, have different initial densities: the farther the particle from the center, the lower its initial density. This leads to their different evolution (Fig. 2): the flame at which the temperature rises to the values at which nuclear reactions begin gradually passes one point after another. The overall expansion of the star gradually reduces the density at all points and, hence, the initial density at which an active nucleosynthesis process is triggered.

The motion of all passive particles together with the medium (and the overall drop in density) is clearly seen on the spatial and temporal temperature and density profiles (Figs. 1 and 2).

The lines connecting the signs indicate the change in burning front characteristics for the entire packet of passive particles under consideration (300). Because of the overall expansion of the star during its burning, this density decreases and in Fig. 2 the time dependences of the medium parameters are shown for the trajectories of the points marked by the signs in Fig. 1. Because of the enhancement of turbulence in the star, the temperature profiles are smeared and the temperature rise in those regions to which the wave arrives later becomes more gradual. These factors lead to a difference in the outcomes of nucleosynthesis along the stellar radius.

Immediately after the explosion the star passes to the regime of expansion. This can be seen on the velocity profiles shown in Fig. 3a. Whereas on short time scales the material near the burning front is drawn into the dynamics, thereafter the material of the entire star moves. Beginning from $t \approx 0.5$ s, the velocity profile becomes close to $v \propto r$. This corresponds to homologous expansion of the star:

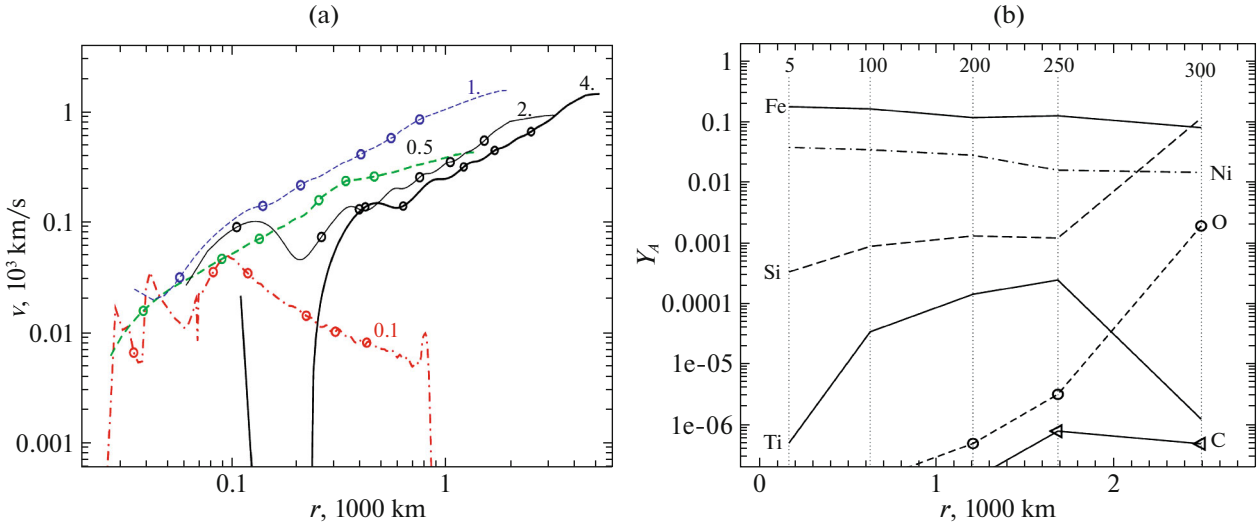

Fig. 3. (a) Velocity profiles in the star at times t from 0.1 to 4 s specified as the line code. The circles mark the values of $V(r)$ for the corresponding trajectories. (b) The spatial distribution of some chemical elements in the remnant ($t = 4$ s): the mass fractions Y_A of iron, carbon, oxygen, silicon, ^{44}Ti, and ^{58}Ni are shown at the end of the trajectories of five passive particles whose positions are indicated by the dashed lines and whose numbers are indicated by the numerals.

behind the wave front the density drops severalfold, which is determined only by the flame microstructure. After $t \approx 2$ s the velocity profile changes already little. The maximum expansion velocity is $\sim$1400 km s^{-1}, corresponding to the deflagration scenario. Thus, the relative distribution of elements at the end of our hydrodynamic calculations ($t = 4$ s) directly shows the propagation of elements in the remnant: it is shown in Fig. 3b. During further expansion this spatial distribution of elements will be retained. The isotopes of iron and nickel are produced most of all among the presented elements. In the envelopes farthest from the center much unburnt carbon and oxygen is preserved, while the amount of titanium, as a product of their burning, decreases.

4. NUCLEOSYNTHESIS

Let us turn to a more detailed description of the second stage—the production of new elements in the burning process. For this purpose, we will use the nucleosynthesis model implemented in the SYNTHEZ code (Blinnikov and Panov 1996; Nadyozhin et al. 1998), which includes all isotopes of the elements from helium ($Z = 2$) to ruthenium ($Z = 44$). It takes into account all pair reactions between all isotopes of these elements and the reactions with neutrons, protons, and α-particles. In addition, this model takes into account the beta-decay and weak-interaction (the interaction of electrons and positrons with nuclei and nucleons) reactions, which was not included in the early versions of the SYNTHEZ code. Weak interactions are important (Cowan et al. 2021) and can change noticeably the ratio of electrons to nucleons and can lead to a change in the course of nucleosynthesis. The thermonuclear reaction rates were calculated using a statistical model (Rauscher and Thielemann 2000) and are based on the predictions of nuclear masses made using a generalized model with a correction of the shell structure (Aboussir et al. 1995). The rates of the remaining weak interactions were taken from other calculations (Langanke and Martinez-Pinedo 2000).

The change in the mass fraction of each nucleus is defined by a differential equation. The large number of equations in the system of nucleosynthesis equations (of the order of a thousand) and the necessity of solving this system during many time steps determine the requirements imposed on the algorithm. The unconditionally stable method of Gear (1971) with a predictor–corrector, an automatic choice of the step and the order of the method that successfully solves the systems of stiff differential equations is implemented in the SYNTHEZ code. Zlatev's algorithm (Østerby and Zlatev 1983) is used to invert the matrices in the calculations. The modified nucleosynthesis model was described in detail previously (Panov et al. 2016).

An example of the time evolution of the chemical composition along one of the trajectories is shown in Fig. 4. It can be seen that some atomic weights (local peaks) stand out among the elements and that the bulk of the mass is concentrated near the iron peak already at the NSE stage. This is related to the energy benefit when passing into iron and close isotopes. Whereas Fig. 4a demonstrates the change in mass fractions as nucleosynthesis passes along a specific trajectory (no. 50), Fig. 4b for several trajectories

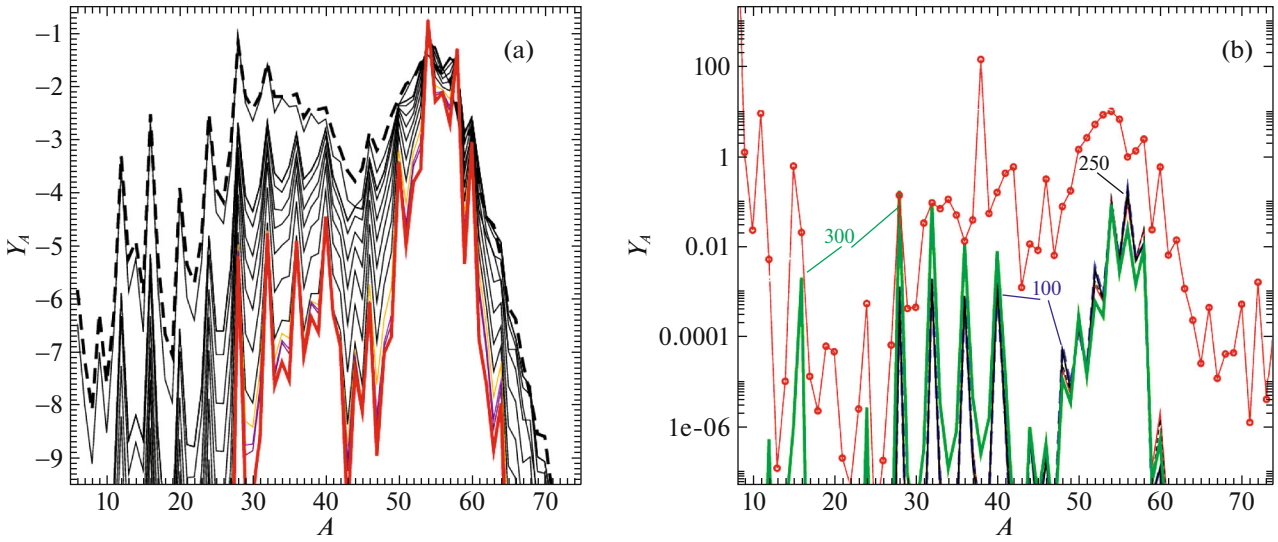

Fig. 4. Evolution of the chemical composition. (a) The time evolution of the abundance of isotopes Y_A along one of the passive particle trajectories (50), i.e., the sum of all mass fractions of the isotopes with an atomic weight A; the initial distribution (at $t = 10^{-6}$ s) is indicated by the dashed line; the final one ($t = 4$ s) is indicated by the thick line. (b) The final abundances of elements Y_A $\left(\sum_i Y_i(A) = 1\right)$ derived in our SN Ia deflagration calculations for different trajectories (the index is the trajectory number); the red circles and the red line represent the abundance observations in the Solar System in relative units.

presents Y_A—the final abundance of isotopes with a mass number A. For the outer trajectory (no. 300) an appreciable amount of oxygen is preserved; for the trajectories starting in deeper regions an enhanced amount of intermediate elements is produced, since the radiation processes when passing deeper trajectories are more intense and inhibit the burnout of light and intermediate elements. The difference in the mass fractions of the iron-peak isotopes produced along different trajectories, as a rule, is smaller, but for lower mass fractions the difference reaches several orders of magnitude.

The farther the Lagrangian point from the stellar center at the initial time, the later the burning wave, behind which a significant rise in temperature begins, reaches it. In this case, due to the overall expansion of the star, the density gradually falls from the very beginning of the SN explosion dynamics. The high temperature and density after the arrival of the burning wave initiate intense nuclear transformations, as a result of which the average atomic number of the elements increases, approaching the iron-peak elements. This process is clearly seen in Fig. 4a, where the evolution of various isotopes is shown with a small time step. The initial time corresponds to nuclear statistical equilibrium (NSE). Subsequently, the fraction of isotopes with $A \lesssim 50$ decreases considerably. At the same time, there is a set of isotopes whose fraction decreases more slowly than the surrounding ones. These include ^{28}Si, ^{32}S, ^{36}Cl, and ^{40}Ca, the most abundant isotopes for these elements. These elements emerge as a result of the reactions running through the α-chain. Therefore, their atomic masses form a sequence with a step of 4 in A.

An appreciable fraction of the isotope ^{28}Si shows that SNe Ia are good sources of silicon. Si II lines are well observed in the spectra of these SNe and are thought to be one of their distinctive features (Filippenko 1997).

Let us present our results in several normalizations, which will allow them to be compared with other data. It should be kept in mind that different scenarios are considered in the calculations: in this paper only the deflagration stage of burning is considered, in other papers detonation can also be taken into account. In this case, much of the nucleosynthesis occurs at high densities, which exactly corresponds to the initial, deflagration stage of burning. For this reason, such a comparison is relevant. Figure 5 presents the integral distribution of elements produced throughout the star normalized to the generalized abundance of elements in the Solar System. Figure 5a shows the integral distributions of elements normalized to the abundance of elements in the Solar System. It can be seen from the figure that the calculated values of Y_A from silicon to nickel agree satisfactorily with the observations. For those elements for which the ratio $Y_A/Y_A^{\rm SS}$ is close to unity (Si, S, Ar, Ca, Ti, V, Cr, ^{56}Fe, Ni), thermonuclear SNe apparently play a prominent role in the process of their production. The calculated amount of the isotope ^{54}Fe exceeds the amount of ^{56}Fe by an order of magnitude. A similar result on the overestimated abundance of the isotope with $A = 54$ was

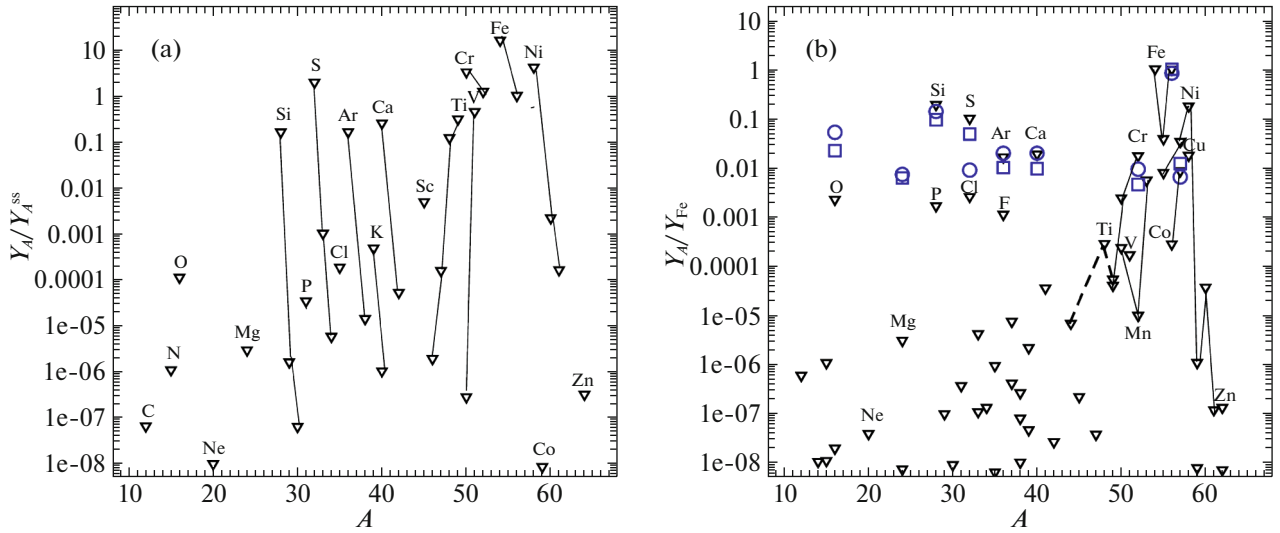

Fig. 5. Calculations of the elemental abundance Y_A: (a) the abundance of chemical elements averaged over the entire star (summed over all trajectories and normalized to the ss abundance); (b) the abundances Y_A normalized to ^{56}Fe (triangles). For comparison, the calculations (Marquardt et al. 2015) of two models with different initial compositions are presented on the right: a NeO core (square) and a C/O core (circles); the lines connect the isotopes of one element.

obtained in our nucleosynthesis calculations (Panov et al. 2016) with the c3-3d-256-10s explosion model (Röpke 2005) and it coincided with the results of Travaglio et al. (2004) and Thielemann et al. (2003). Most likely, the reason has to do with the database of reaction rates used or the codes of their processing. For the remaining ones there are other objects where their nucleosynthesis occurs.

The dependence of the yield of elements on the atomic mass A of nuclei normalized to the iron yield is shown in Fig. 5b. This representation allows us to make a comparison with other calculations (Marquardt et al. 2015). The calculations of the abundances of elements from Si to Ca are in good agreement. The abundances of iron-peak nuclei are more difficult to compare, since only the most abundant isotopes are presented in Marquardt et al. (2015).

As a result of nuclear reactions, the bulk of the material passes into isotopes with atomic numbers $A = 50$–60 near the iron peak.

Note that the results of our calculations presented in Fig. 5b are also in satisfactory agreement with the results of the calculations of other authors (Travaglio et al. 2004; Maeda et al. 2010), although the SN progenitor models and the nuclear data for nucleosynthesis were different. Note that the results normalized to the observational data in Travaglio et al. (2004) are presented in solar masses (whereas on our plots they are presented in relative units and were obtained only for a selected set of trajectories). Note also that the previous calculations based on our nucleosynthesis model (Panov et al. 2018), in which the 3D c3-3d-256-10s model (Röpke 2005) was used as basic hydrodynamic calculations, gave approximately equal (in order of magnitude) amounts of ^{54}Fe–^{56}Fe.

5. CONCLUSIONS

An analysis of the details of the formation and propagation of a burning wave and the subsequent ejection of outer layers so far gives no unequivocal answer to the question of what the conditions for explosive nucleosynthesis, which is the main process of the production of elements from carbon to iron and nickel, are. Therefore, a detailed study of SNe of various types, including those with or without helium and hydrogen envelopes, is important. The parameters of the burning wave arising during a white dwarf explosion were studied within the hydrodynamic model. They are needed to understand the pattern of change in the density and temperature profiles; knowing their time dependence allows nucleosynthesis calculations to be performed.

In this paper we considered nucleosynthesis for a number of typical trajectories during a thermonuclear SN explosion derived through simulations by the FRONT3D code. The main results are as follows: predominantly iron-peak elements are produced during the deflagration of a carbon–oxygen mixture in the regions heated by the burning wave to temperatures $T_9 > 5$. Elements from oxygen to calcium are produced in the outer layers, but in smaller quantities. This difference is probably explained by the absence of a detonation stage. Although the results obtained based on the extended nucleosynthesis model and the trajectories of passive particles showed satisfactory agreement with other realizations of the white dwarf

explosion scenario and the calculations of other authors for a number of chemical elements, we consider them as preliminary ones. The work both to refine the reaction rates under rapidly changing explosive nucleosynthesis conditions and to further develop the model of the deflagration–detonation regime of burning development lies ahead. The (n, γ) and (γ, n) reaction rates will be refined and the initial reaction rates from different data sources will be checked. This will allow one to study various types of SNe, to perform a more detailed quantitative analysis of the elements being produced, and to better understand the dynamics of the emergence of chemical elements in the Universe.

One of the interesting problems affecting the formation of the abundances of elements from carbon to iron and nickel in the Universe is a comparison of the results of nucleosynthesis during a white dwarf explosion and nucleosynthesis in the envelopes of a massive SN progenitor that lost a significant fraction of helium and hydrogen (type Ic) on the path of evolution, whose spectrum does not show any silicon absorption lines, in contrast to SNe Ia. Searching for the causes of a significant difference in the relative mass fractions of magnesium and silicon will be one of the goals of our further work.

ACKNOWLEDGMENTS

We are grateful to S.I. Blinnikov, V.P. Utrobin, and E.I. Sorokina for the discussion of SN explosion models and to the anonymous referee for the useful remarks.

FUNDING

This work was supported by the Russian Foundation for Basic Research (project no. 21-52-12032 NNIO_a).

REFERENCES

1. Y. Aboussir, J. M. Pearson, A. K. Dutta, and F. Tondeur, At. Data Nucl. Data Tabl. **61**, 127 (1995).
2. S. I. Blinnikov and I. V. Panov, Astron. Lett. **22**, 39 (1996).
3. J. J. Cowan, C. Sneden, J. E. Lawler, A. Aprahamian, M. Wiescher, K. Langanke, G. Martínez-Pinedo, and F.-K. Thielemann, Rev. Mod. Phys. **93**, 015002 (2021).
4. A. V. Filippenko, Ann. Rev. Astron. Astrophys. **35**, 309 (1997).
5. C. W. Gear, *Numerical Initial Value Problems in Ordinary Differential Equations* (Prentice-Hall, Englewood Cliffs, NJ, 1971).
6. S. I. Glazyrin, Astron. Lett. **39**, 221 (2013).
7. S. I. Glazyrin, Astrophys. Space Sci. **350**, 683 (2014).
8. W. Hillebrandt and J. C. Niemeyer, Ann. Rev. Astron. Astrophys. **38**, 191 (2000).
9. I. Iben, Jr. and A. V. Tutukov, Astrophys. J. Suppl. Ser. **54**, 335 (1984).
10. A. M. Khokhlov, Astrophys. J. **449**, 695 (1995).
11. L. D. Landau, Zh. Eksp. Teor. Fiz. **14**, 240 (1944).
12. K. Langanke and G. Martínez-Pinedo, Nucl. Phys. A **673**, 481 (2000).
13. K. Maeda, F. K. Röpke, M. Fink, W. Hillebrandt, C. Travaglio, and F.-K. Thielemann, Astrophys. J. **712**, 624 (2010).
14. K. S. Marquardt, S. A. Sim, A. J. Ruiter, I. R. Seitenzahl, S. T. Ohlmann, M. Kromer, R. Pakmor, and F. K. Ropke, Astron. Astrophys. **580**, A118 (2015).
15. A. Nonaka, A. J. Aspden, M. Zingale, A. S. Almgren, J. B. Bell, amd S. E. Woosley, Astrophys. J. **745**, 73 (2012).
16. O. Østerby and Z. Zlatev, *Direct Methods for Sparse Matrices,* Vol. 157 of *Lecture Notes in Computer Science* (Springer, Berlin, 1983).
17. I. V. Panov, I. Yu. Korneev, S. I. Blinnikov, and F. Roepke, JETP Lett. **103**, 431 (2016).
18. I. V. Panov, S.I. Glazyrin, F. Röpke, S. I. Blinnikov, Astron. Lett. **44**, 309 (2018).
19. T. Rauscher and F.-K. Thielemann, At. Data Nucl. Data Tabl. **75**, 1 (2000).
20. L. Rayleigh, Proc. London Math. Soc. **14**, 170 (1883).
21. M. Reinecke, W. Hillebrandt, and J. C. Niemeyer, Astron. Astrophys. **347**, 739 (1999).
22. F. K. Röpke, Astron. Astrophys. **432**, 969 (2005).
23. V. A. Simonenko, D. A. Gryaznykh, N. G. Karlykhanov, et al., Astron. Lett. **33**, 80 (2007).
24. G. I. Taylor, Proc. R. Soc. London, Ser. A **201**, 192 (1950).
25. F.-K. Thielemann, D. Argast, F. Brachwitz, W.R. Hix, P. Hoflich, M. Liebendorfer, G. Martinez-Pinedo, A. Mezzacappa, I. Panov, and T. Rauscher, in *From Twilight to Highlight: The Physics of Supernovae, Proceedings of the ESO/MPA/MPE Workshop, Garching, Germany* (2003), p. 331.
26. F. X. Timmes and S. E. Woosley, Astrophys. J. **396**, 649 (1992).
27. C. Travaglio, W. Hillebrandt, M. Reinecke, and F.-K. Thielemann, Astron. Astrophys. **425**, 1029 (2004).
28. R. F. Webbink, in *Proceedings of IAU Colloq. 53, Rochester, NY, July 30–August 2, 1979,* Ed. by H. M. van Horn and V. Weidemann (Univ. Rochester, 1979), p. 426.
29. R. F. Webbink, Astrophys. J. **277**, 355 (1984).
30. J. Whelan and I. Iben, Jr., Astrophys. J. **186**, 1007 (1973).

Translated by V. Astakhov